Featured in Physics

Curvature-Regulated Multiphase Patterns in Tori

Ting Wang,[1,2] Zhijun Dai,[1] Michel Potier-Ferry,[3] and Fan Xu[1,*]
[1]Institute of Mechanics and Computational Engineering, Department of Aeronautics and Astronautics, Fudan University, Shanghai 200433, People's Republic of China
[2]Laboratoire de Physique de l'Ecole normale supérieure, ENS, Université PSL, CNRS, Sorbonne Université, Université de Paris, F-75005 Paris, France
[3]Université de Lorraine, CNRS, Arts et Métiers ParisTech, LEM3, F-57000 Metz, France

(Received 4 April 2022; accepted 5 December 2022; published 25 January 2023)

Biological functions in living systems are closely related to their geometries and morphologies. Toroidal structures, which widely exist in nature, present interesting features containing positive, zero, and negative Gaussian curvatures within one system. Such varying curvatures would significantly affect the growing or dehydrating morphogenesis, as observed in various intricate patterns in abundant biological structures. To understand the underlying morphoelastic mechanism and to determine the crucial factors that govern the patterning in toroidal structures, we develop a core-shell model and derive a scaling law to characterize growth- or dehydration-induced instability patterns. We find that the eventual patterns are mainly determined by two dimensionless parameters that are composed of stiffness and curvature of the system. Moreover, we construct a phase diagram showing the multiphase wrinkling pattern selection in various toroidal structures in terms of these two parameters, which is confirmed by our experimental observations. Physical insights into the multiphase transitions and existence of bistable modes are further provided by identifying hysteresis loops and the Maxwell equal-energy conditions. The universal law for morphology selection on core shell structures with varying curvatures can fundamentally explain and precisely predict wrinkling patterns of diverse toroidal structures, which may also provide a platform to design morphology-related functional surfaces.

DOI: 10.1103/PhysRevLett.130.048201

The mysterious wavy patterns in the natural world attract many researchers to investigate their biological functions and physical origins [1–5]. Morphogenesis can be affected by many intrinsic and external factors, often associated with spontaneous symmetry breaking [6–8]. Along with constituent properties [9,10] and external stimuli [11–14], geometry is one of the most important physical factors, for which curvature is a typical feature [15,16]. A cylindrical core shell structure can exhibit axisymmetric sinusoidal to nonaxisymmetric diamondlike pattern transition under excess axial compression [17,18], while a spherical core shell system upon shrinkage may experience a buckyball pattern (periodic pentagons and hexagons) to labyrinth transformation [9,10,15]. Uniaxially compressed bilayer systems with negative Gaussian curvature promote a sinusoidal or diamondlike mode transition [19]. Apart from uniformly curved surfaces such as sphere and cylinder, the interesting toroidal geometry, which can be considered as the bent or branched tubular structures introducing curvature in the second principal directions, contains regions with positive, zero, and negative Gaussian curvatures. In nature, many biological tissues have core-shell structures with such nonconstant curvatures, and exhibit inherently different wrinkling morphologies compared to the surfaces with more uniform curvatures (see Fig. 1). Geometries with nonuniform curvatures are ubiquitous in nature, but theoretical understanding and prediction of their nonlinear instability are quite challenging. Why do instability patterns on nonuniformly curved surfaces differ from the ones on uniform geometries? How do varying curvatures influence the morphology patterns? These questions remain elusive.

The toroidal system that integrates positive, zero, and negative Gaussian curvatures into one configuration can be considered as an ideal platform to explore in a single system the morphological pattern selection and transition affected by varying curvatures. In this work, we systematically develop a core-shell model based on general differential geometry and derive a scaling law that can effectively account for the complex wrinkling process on toroidal surfaces. We reveal that in toroidal geometry with nonuniform curvatures, pattern selection becomes much more complicated, usually with coexistent multiphases. We draw a universal phase diagram of their surface topographies determined by two dimensionless parameters in a wide range of parameter space, which are also confirmed by our demonstrative experiments.

We first develop a general toroidal core-shell model [21] based on differential geometry. Curvilinear coordinates (θ_1, θ_2) are adopted for the toroidal shell with radii R

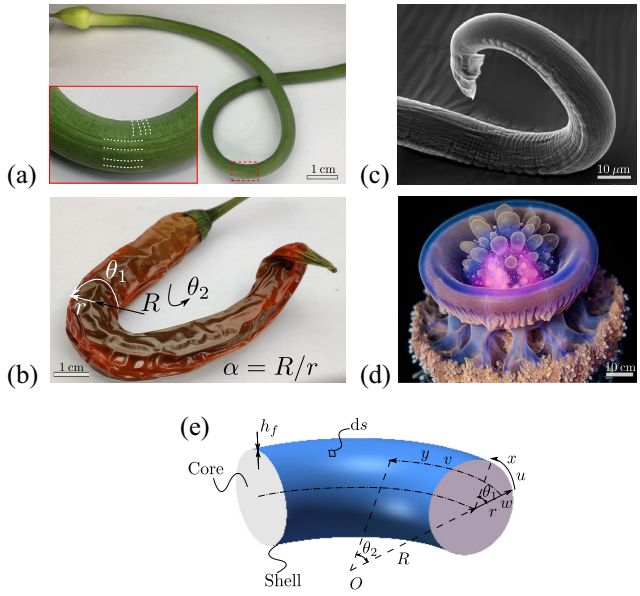

FIG. 1. Surface wrinkling morphologies in various living matter with toroidal geometry. (a) Bidirectional stripes on a garlic. (b) Hexagonal-labyrinth bistable patterns on a dehydrated pepper. (c) Transverse and longitudinal wrinkles on an adult male *Caenorhabditis elegans*. Image obtained through SEM by Carolyn Marks and David Hall of the Hall Lab in WormAtlas [20]. (d) Wrinkles in Crown jellyfish; photo by Jason Webb. (e) Geometry of a core-shell torus.

and r, where R denotes distance from the center of the torus to the axes of the shell with a radius r [see Fig. 1(e)]. The total elastic potential energy Π_f of the surface layer can be written as the sum of stretching energy Π_m and bending energy Π_b [28,29], which is different from the Canhan-Helfrich model only involving bending energy but no stretching energy [30,31]:

$$\begin{aligned}\Pi_f &= \Pi_m + \Pi_b \\ &= \frac{J}{2}\int_{\theta_2}\int_{\theta_1}[\varepsilon_{11}^2 + \varepsilon_{22}^2 + 2\nu\varepsilon_{11}\varepsilon_{22} + 2(1-\nu)\varepsilon_{12}^2]ds \\ &\quad + \frac{D}{2}\int_{\theta_2}\int_{\theta_1}[\kappa_{11}^2 + \kappa_{22}^2 + 2\nu\kappa_{11}\kappa_{22} + 2(1-\nu)\kappa_{12}^2]ds,\end{aligned} \tag{1}$$

where $J = E_f h_f/(1-\nu^2)$ and $D = E_f h_f^3/[12(1-\nu^2)]$ represent, respectively, the extensional rigidity and bending stiffness of the shell, and $ds = r(R + r\cos\theta_1)d\theta_1 d\theta_2$ stands for the differential element area. Young's modulus, thickness, and Poisson's ratio of the shell are denoted by E_f, h_f, and ν, respectively. We consider a Winkler-type foundation [32,33] for the elastic behavior of the core, and its potential energy reads

$$\Pi_s = \frac{1}{2}\int_{\theta_2}\int_{\theta_1} K_s w^2 ds, \tag{2}$$

in which w is the deflection and K_s denotes the effective stiffness of the core, satisfying the order of magnitude $K_s \sim E_s/\ell$, where ℓ is the half buckling wavelength [32].

We further perform dimensional analysis of the potential energies (1) and (2) to find the crucial factors that determine wrinkling topography. Assuming that the deflection w is the same order of the thickness h_f and the in-plane displacements (u, v) remain much smaller, in order of h_f^2/r, the following dimensionless coordinates and kinematic variables are introduced,

$$(x, y) = \ell(\bar{x}, \bar{y}), \qquad (u, v) = \frac{h_f^2}{r}(\bar{u}, \bar{v}), \qquad w = h_f\bar{w}, \tag{3}$$

where x and y are arclengths. For a toroidal shell without a core, the half buckling wavelength ℓ can be obtained by assuming the bending energy and membrane energy in the same order. Considering $\kappa \sim \partial^2 w/\partial x^2$, one obtains $\Pi_b/\ell^2 \sim E_f h_f^3 \kappa^2 \sim E_f h_f^5/\ell^4$ and $\Pi_m/\ell^2 \sim E_f h_f (w/r)^2 \sim E_f h_f^3/r^2$. Comparing the orders of magnitude of the bending and membrane energies yields the critical wrinkling wavelength ℓ:

$$\frac{E_f h_f^5}{\ell^4} \sim \frac{E_f h_f^3}{r^2} \Rightarrow \ell \sim \sqrt{r h_f}. \tag{4}$$

Considering a thin shell with $h_f/r \ll 1$ and neglecting higher-order terms yields the leading orders of magnitude of strain and curvature tensors [21]:

$$\varepsilon_{\alpha\beta} \sim \frac{h_f}{r}, \qquad \kappa_{\alpha\beta} \sim \frac{1}{r}, \tag{5}$$

where the subscript greek indices $\{\alpha, \beta\} \in \{1, 2\}$. Substituting Eq. (5) to the potential energies (1) and (2) leads to the orders of magnitude of energies:

$$\frac{\Pi_f}{\ell^2} \sim \frac{E_f h_f^3}{r^2}, \qquad \frac{\Pi_s}{\ell^2} \sim K_s h_f^2. \tag{6}$$

Comparing both energies naturally leads to a dimensionless parameter that measures the relative stiffness and curvature:

$$C_s = \frac{K_s}{E_f}\frac{r^2}{h_f}. \tag{7}$$

Notably, this dimensionless parameter C_s together with the radius ratio α can characterize a wide range of morphological pattern selection in core-shell tori.

To explore morphological formation and evolution of toroidal core shell structures, we apply the finite element method that couples shell element for the surface layer and spring element for the soft core [21]. The dehydration process results in strain mismatch between the surface layer and the substrate, and thus we apply thermal mismatch load

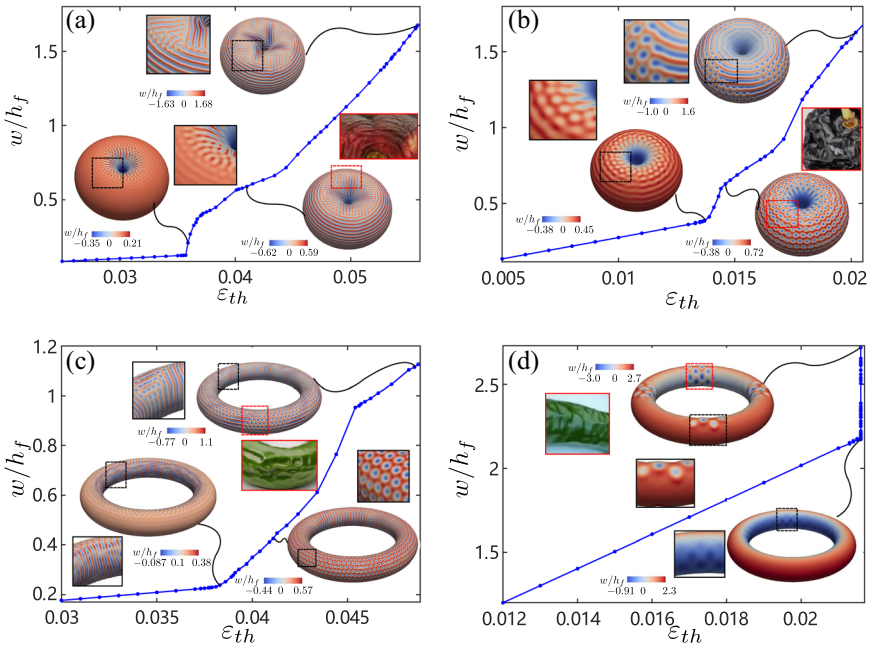

FIG. 2. Bifurcation diagrams of diverse toroidal core shell structures. (a) A cherrylike torus ($\alpha = 1.1$ and $C_s = 81$). Axisymmetric stripes appear in the outside region of torus, while spiral stripes emerge in the inner region. The inset in red box indicates axisymmetric stripes on a peach. (b) A cherrylike torus with a soft core ($\alpha = 1.1$ and $C_s = 8.1$). A hexagonal to labyrinthlike topography transition, associated with a bistable phase, is observed in the postbuckling regime. The inset in red box shows hexagons on a shrinking cherry. (c) A donutlike torus ($\alpha = 5$ and $C_s = 16$). Stripes emerge in the inner region initially, yet hexagonal pattern prevails on the outer surface and eventually evolves into labyrinthlike topography. The inset in red box illustrates hexagonal-labyrinth bistable patterns on a dehydrated pepper. (d) A donutlike torus with a soft core ($\alpha = 5$ and $C_s = 0.16$). Localized dimples are observed. The inset in red box demonstrates dimples on a dehydrated pepper. The spatial point on the core-shell surface with maximum deflection at the final incremental step is chosen for each bifurcation curve.

between the shell and the core [21]. The heterogeneity of stress distribution in the prebuckling stage due to varying curvatures in toroidal geometry is a physical "motor" to induce symmetry-breaking instability and pattern transition.

We look into the effects of varying curvatures on wrinkling topography of toroidal core shell structures according to the key parameters α and C_s. The radius ratio α determines the spatial topology; i.e., small value ($\alpha \sim 1$) approximates to a sphere [Figs. 2(a) and 2(b)] while large value represents a torus. For the former one with a stiff core [e.g., $C_s = 81$ in Fig. 2(a)], axisymmetric stripes emerge in the outside region with positive Gaussian curvature, while spiral stripes appear in the inner region with negative Gaussian curvature. We next consider a torus with a soft core and set $C_s = 8.1$. Instead of the stripe mode observed in the stiff core case, hexagonal topography dominates in the outside region. With further loading, a mode transition from hexagonal to labyrinthlike patterns associated with a bistable phase is observed in Fig. 2(b).

We next explore donutlike tori with relatively large radius ratio ($\alpha = 5$). For a torus with a stiff core ($C_s = 16$), stripes along the θ_1 direction in the inner region occur initially, as illustrated in Fig. 2(c). Upon further loading, hexagonal pattern emerges on the outer surface, and eventually evolves into labyrinthlike topography. For the donutlike torus with a soft core ($C_s = 0.16$), localized dimples emerge on the inner surface at the critical threshold [see Fig. 2(d)]. In general, for the donutlike torus with large α, instability is prone to appear first in the region with negative Gaussian curvature.

To provide an overall view of complex multiphase wrinkling morphologies of various toroidal structures, we draw in Fig. 3 a phase diagram of pattern selection in terms of C_s and α, which determines pattern selections in a wide range of parameter space [21]. The core-shell tori with small $C_s < 1$ tend to deform to localized dimples (blue region), while bidirectional stripe topography (orange region) and spiral and axisymmetric coexistent stripe morphology (purple region) prevail in core-shell tori with larger $C_s > 10$. For a moderate C_s in between, periodic hexagons (red region) and symmetry-breaking hexagonal-labyrinth coexistent patterns (green region) appear to be energetically favorable. To confirm such curvature-affected morphogenesis predicted by our numerical predictions, we design a series of demonstrative experiments by using polydimethylsiloxane (PDMS) coated elastomer that can shrink at decreasing temperature or swell in a compatible organic solvent such as hexanes [21]. We apply 3D printing technology to construct toroidal molds made of photopolymer resin with different radius ratios α, which are then

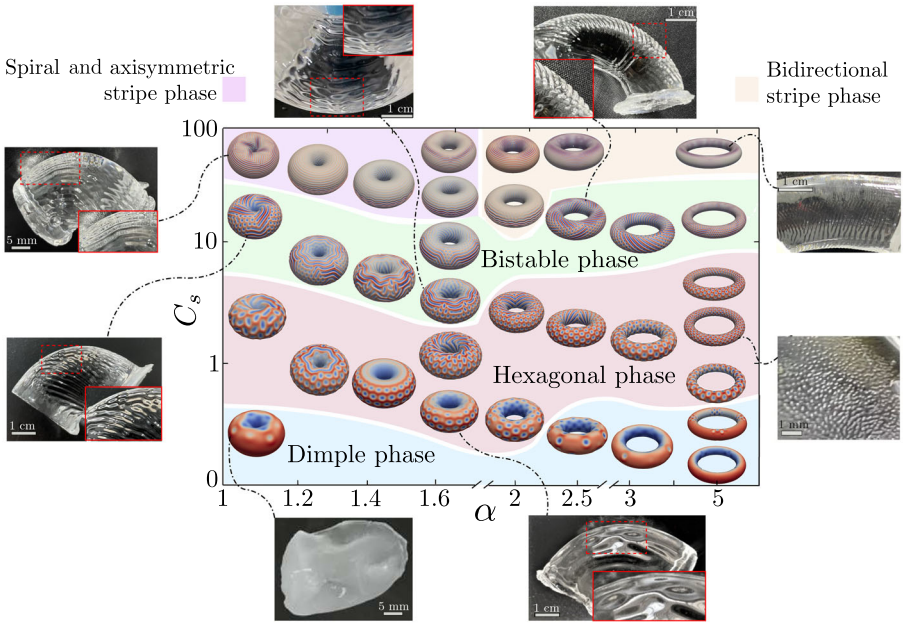

FIG. 3. Phase diagram of wrinkling morphologies in a variety of core-shell structures, consistent with experimental observations. Localized dimples (blue region) appear in core shell systems with small $C_s < 1$, while bidirectional stripe topography (orange region) and spiral and axisymmetric coexistent stripe morphology (purple region) dominate in core shell systems with larger $C_s > 10$. Periodic hexagonal patterns (red region) and hexagonal-labyrinth bistable modes (green region) are favorable in between.

used to cast the core of torus with silicone-based elastomers, such as gel and PDMS (Sylgard 184, Dow Corning). We then adopt PDMS base that is homogeneously mixed with cross-linker at a 10∶1 mass ratio to uniformly pour on the toroidal core for making the surface layer. Upon thermal shrinkage or chemical swelling in hexanes, a variety of surface morphologies form (see Fig. 3). Experimental morphology evolutions show a high consistency with dehydrating fruits and numerical predictions [21].

To further explore the underlying mechanism of intriguing smooth-hexagonal-labyrinth transitions [see Fig. 2(b)], we look into a complete loading-unloading cycle in computations. The maximum deflections are plotted in Figs. 4(a) and 4(b), where the progression along the curves in the loading and unloading segments of the path history is indicated by the direction of the arrows. Upon thermal load, periodic hexagons emerge at $\varepsilon_{s\to h} = 0.0147$. With further loading, a bistable phase transition with hexagonal and labyrinth modes coexisting in this interval occurs, and labyrinth prevails when the strain reaches $\varepsilon_{h\to l} = 0.0194$. During unloading, the labyrinth reverts back to the hexagons again at $\varepsilon_{l\to h} = 0.0153$. With further unloading, the hexagons return to the smooth at a smaller overall strain $\varepsilon_{h\to s} = 0.011$, compared with loading stage ($\varepsilon_{s\to h} = 0.0147$). Viewing the whole unloading process, two hysteresis loops are found within the smooth-hexagonal and hexagonal-labyrinth transition stages. There is obvious hysteresis with smooth prevailing during loading and hexagons dominating during unloading in the range $\varepsilon_{h\to s} < \varepsilon_{th} < \varepsilon_{s\to h}$ [see Fig. 4(a)]. Similarly, hexagonal-labyrinth transitions in Fig. 4(b) are governed by two critical values, $\varepsilon_{l\to h}$ and $\varepsilon_{h\to l}$. Yet it is still difficult to judge what happened during smooth-hexagonal or hexagonal-labyrinth coexistent stages.

Further insights into the coexistence of bistable phases can be obtained from examining the differences in the elastic energy in the core shell structures between the loading and unloading states, $U_{\rm lo} - U_{\rm ul}$, associated with hysteresis cycles. Pattern transitions in the postbuckling regime generally imply the change of energy states. We first focus on smooth-hexagonal transformations. When the energies of the smooth state U_s and the hexagonal state U_h share the same value of an overall strain, it is defined as the Maxwell strain $\varepsilon^{sh}_{\rm Max}$ [34]. In the smooth-hexagonal transition region, the hexagonal state has a higher energy than the smooth state ($U_h - U_s > 0$) when the overall strain is lower than the Maxwell strain ($\varepsilon_{th} < \varepsilon^{sh}_{\rm Max}$), while the hexagonal state has a lower energy ($U_h - U_s < 0$) when $\varepsilon_{th} > \varepsilon^{sh}_{\rm Max}$ [see Fig. 4(c)]. The smooth phase is stable when $\varepsilon_{th} < \varepsilon^{sh}_{\rm Max}$, and the hexagonal solution existing in this range remains subcritical. At the Maxwell condition ($\varepsilon_{th} = \varepsilon^{sh}_{\rm Max}$), the smooth state and the hexagonal state hold the same energy and, in principle, can coexist. Under such conditions, if ε_{th} is then increased above $\varepsilon^{sh}_{\rm Max}$, the hexagonal mode prevails, while if ε_{th} is reduced below $\varepsilon^{sh}_{\rm Max}$, the smooth state dominates engulfing the hexagons. The energy in hexagonal phase remains asymptotically constant in the range $\varepsilon^{sh}_{\rm Max} < \varepsilon_{th} < \varepsilon^{hl}_{\rm Max}$, which suggests that hexagonal solutions are stable within this interval. A similar mechanism is observed for hexagonal-labyrinth transitions

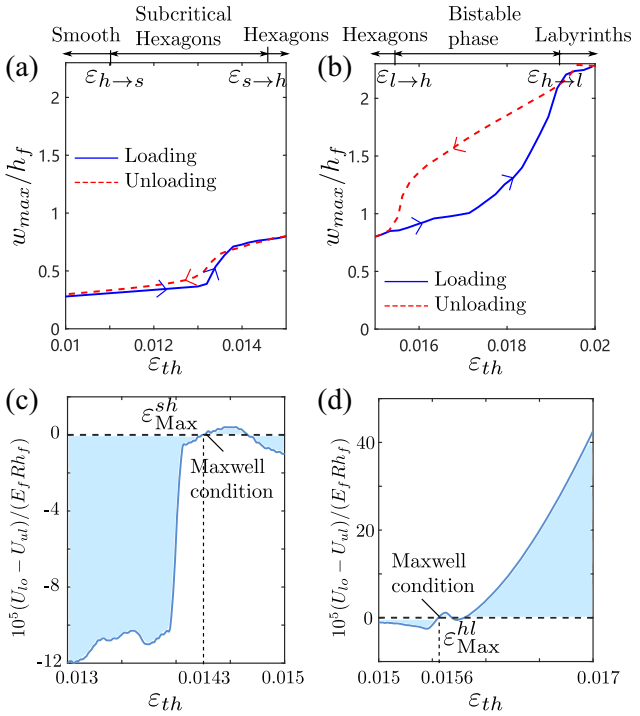

FIG. 4. Comparison between loading and unloading stages ($\alpha = 1.1$ and $C_s = 8.1$). The top row shows the deflections $w_{\max}/h_f$ as a function of overall strain ε_{th} within hysteresis loops: (a) smooth-hexagonal transition, (b) hexagonal-labyrinth transition. Panels (c) and (d) demonstrate the elastic energy differences between the loading and unloading states, $U_{\rm lo} - U_{\rm ul}$, as a function of overall strain ε_{th}, corresponding to (a) and (b), respectively. In the range $\varepsilon_{h\to s} < \varepsilon < \varepsilon_{s\to h}$ ($U_{\rm lo} - U_{\rm ul} = U_s - U_h$) and $\varepsilon_{l\to h} < \varepsilon < \varepsilon_{h\to l}$ ($U_{\rm lo} - U_{\rm ul} = U_h - U_l$), the Maxwell equal-energy conditions are defined by the points when $U_{\rm lo} - U_{\rm ul} = 0$.

in Fig. 4(d), where the Maxwell strain $\varepsilon^{hl}_{\rm Max} = 0.0156$, associated with that the energy of the hexagonal state U_h equals to the labyrinth state U_l, i.e., $U_h - U_l = 0$, which explains the coexistence of hexagonal and labyrinth phases.

In summary, we have uncovered the postbuckling evolution and morphological pattern transitions of toroidal core shell structures omnipresent in nature. A remarkable finding lies in a universal law that determines complex wrinkling topography on diverse tori with varying Gaussian surfaces and interprets the biophysical interplay between geometry and material stiffness on multiphase pattern selection, confirmed by our carefully designed experiments. Notably, we have revealed that donutlike tori ($\alpha > 2$) are prone to initially wrinkle in the inner region with negative Gaussian curvature, yet cherrylike tori ($\alpha < 2$) favor to wrinkle in the outer region with positive Gaussian curvature [21]. A dimensionless parameter C_s that characterizes the stiffness ratio and geometric curvature of core shell structures is found to determine the eventual instability topography. Localized dimples are preferable in core-shell tori with $C_s < 1$, while bidirectional stripe or spiral and axisymmetric coexistent stripe is favorable in core-shell tori with $C_s > 10$. For a moderate C_s in between, periodic hexagons and symmetry-breaking hexagonal-labyrinth coexistent patterns prevail. Local wrinkling pattern selection in nontoroidal geometry such as S-shaped core shell systems [21] can also be well predicted by the phase diagram based on the local values of both dimensionless parameters, which suggests that our theory is universal and can be applicable to a large class of core-shell systems (e.g., see Fig. 1). Hysteresis loops and the Maxwell equal-energy conditions provide physical insights into smooth-hexagonal and hexagonal-labyrinth transitions. Understanding the configurational curvature effects on nonuniform morphological pattern formation in core-shells and the ability of determining multiphase selection can shed light on designs of multifunctional surfaces based on wrinkling topography.

This work is supported by the National Natural Science Foundation of China (Grants No. 12122204 and No. 11872150), Shanghai Pilot Program for Basic Research-Fudan University (Grant No. 21TQ1400100-21TQ010), Shanghai Shuguang Program (Grant No. 21SG05), and young scientist project of Ministry of Education innovation platform. M. P.-F. acknowledges the financial support from the French National Research Agency ANR (LabEx DAMAS, Grant No. ANR-11-LABX-0008-01).

*Corresponding author.
fanxu@fudan.edu.cn

[1] E. Sharon, B. Roman, M. Marder, G.-S. Shin, and H. L. Swinney, Nature (London) **419**, 579 (2002).
[2] E. Cerda and L. Mahadevan, Phys. Rev. Lett. **90**, 074302 (2003).
[3] E. Sharon, B. Roman, and H. L. Swinney, Phys. Rev. E **75**, 046211 (2007).
[4] J. Dervaux and M. Ben Amar, Phys. Rev. Lett. **101**, 068101 (2008).
[5] H. Liang and L. Mahadevan, Proc. Natl. Acad. Sci. U.S.A. **108**, 5516 (2011).
[6] F. Brau, H. Vandeparre, A. Sabbah, C. Poulard, A. Boudaoud, and P. Damman, Nat. Phys. **7**, 56 (2011).
[7] T. Tallinen, J. Y. Chung, F. Rousseau, N. Girard, J. Lefèvre, and L. Mahadevan, Nat. Phys. **12**, 588 (2016).
[8] M. Holland, S. Budday, A. Goriely, and E. Kuhl, Phys. Rev. Lett. **121**, 228002 (2018).
[9] B. Li, F. Jia, Y.-P. Cao, X.-Q. Feng, and H. Gao, Phys. Rev. Lett. **106**, 234301 (2011).
[10] F. Xu, S. Zhao, C. Lu, and M. Potier-Ferry, J. Mech. Phys. Solids **137**, 103892 (2020).
[11] J. Yin, Z. Cao, C. Li, I. Sheinman, and X. Chen, Proc. Natl. Acad. Sci. U.S.A. **105**, 19132 (2008).
[12] M. Ben Amar and F. Jia, Proc. Natl. Acad. Sci. U.S.A. **110**, 10525 (2013).
[13] P. Ciarletta, V. Balbi, and E. Kuhl, Phys. Rev. Lett. **113**, 248101 (2014).

[14] F. Xu, C. Fu, and Y. Yang, Phys. Rev. Lett. **124**, 038003 (2020).
[15] N. Stoop, R. Lagrange, D. Terwagne, P. M. Reis, and J. Dunkel, Nat. Mater. **14**, 337 (2015).
[16] M. Pezzulla, N. Stoop, M. P. Steranka, A. J. Bade, and D. P. Holmes, Phys. Rev. Lett. **120**, 048002 (2018).
[17] Y. Zhao, Y. Cao, X.-Q. Feng, and K. Ma, J. Mech. Phys. Solids **73**, 212 (2014).
[18] F. Xu and M. Potier-Ferry, J. Mech. Phys. Solids **94**, 68 (2016).
[19] Y. Zhao, W. Guo, H. Zhu, Y. He, C. Jiang, and Y. Cao, J. Mech. Phys. Solids **154**, 104516 (2021).
[20] C. Marks and D. Hall, In WormAtlas, http://www.wormatlas.org.
[21] See Supplemental Material at http://link.aps.org/supplemental/10.1103/PhysRevLett.130.048201 for the movie of pattern evolutions, details on theoretical derivations, numerical simulations, and experimental methods with further results and discussions about curvature and constitutive effects on wrinkling topography, which includes Refs. [22–27].
[22] P. G. Ciarlet, J. Elast. **78**, 1 (2005).
[23] Abaqus, *ABAQUS Analysis User's Manual, Version 6.13* (2013).
[24] C. Huang, Z. Wang, D. Quinn, S. Suresh, and K. J. Hsia, Proc. Natl. Acad. Sci. U.S.A. **115**, 12359 (2018).
[25] J. N. Lee, C. Park, and G. M. Whitesides, Anal. Chem. **75**, 6544 (2003).
[26] E. Favre, P. Schaetzel, Q. T. Nguygen, R. Clément, and J. Néel, J. Membr. Sci. **92**, 169 (1994).
[27] T. Tallinen, J. Y. Chung, J. S. Biggins, and L. Mahadevan, Proc. Natl. Acad. Sci. U.S.A. **111**, 12667 (2014).
[28] N. Yamaki, *Elastic Stability of Circular Cylindrical Shells* (North-Holland, Amsterdam, 1984).
[29] A. M. A. van der Heijden, *W.T. Koiter's Elastic Stability of Solids and Structures* (Cambridge University Press, New York, 2009).
[30] J.-M. Allain, C. Storm, A. Roux, M. Ben Amar, and J.-F. Joanny, Phys. Rev. Lett. **93**, 158104 (2004).
[31] J.-M. Allain and M. Ben Amar, Eur. Phys. J. E **20**, 409 (2006).
[32] M. Biot, J. Appl. Mech. **203**, A1 (1937).
[33] H. G. Allen, *Analysis and Design of Structural Sandwich Panels* (Pergamon Press, New York, 1969).
[34] G. W. Hunt, M. A. Peletier, A. R. Champneys, P. D. Woods, M. Ahmer Wadee, C. J. Budd, and G. J. Lord, Nonlinear Dyn. **21**, 3 (2000).